Post-Tanner spreading of nematic droplets

S Mechkov[1], A M Cazabat[2] and G Oshanin[1,3]

[1] Laboratoire de Physique Théorique de la Matière Condensée, Université Pierre et Marie Curie, 4 place Jussieu, 75252 Paris Cedex 5, France
[2] Laboratoire de Physique Statistique, Ecole Normale Supérieure, 75252 Paris Cedex 5, France
[3] Laboratory J-V Poncelet (UMI CNRS 2615), Independent University of Moscow, Bolshoy Vlasyevskiy Pereulok 11, 119002 Moscow, Russia

E-mail: mechkov@lptmc.jussieu.fr, anne-marie.cazabat@lps.ens.fr and oshanin@lptmc.jussieu.fr

Abstract
The quasistationary spreading of a circular liquid drop on a solid substrate typically obeys the so-called Tanner law, with the instantaneous base radius $R(t)$ growing with time as $R \sim t^{1/10}$—an effect of the dominant role of capillary forces for a small-sized droplet. However, for droplets of nematic liquid crystals, a *faster* spreading law sets in at long times, so that $R \sim t^{\alpha}$ with α significantly larger than the Tanner exponent $1/10$. In the framework of the thin film model (or lubrication approximation), we describe this 'acceleration' as a transition to a qualitatively different spreading regime driven by a strong substrate–liquid interaction specific to nematics (antagonistic anchoring at the interfaces). The numerical solution of the thin film equation agrees well with the available experimental data for nematics, even though the non-Newtonian rheology has yet to be taken into account. Thus we complement the theory of spreading with a post-Tanner stage, noting that the spreading process can be expected to cross over from the usual capillarity-dominated stage to a regime where the whole reservoir becomes a diffusive film in the sense of Derjaguin.

(Some figures in this article are in colour only in the electronic version)

1. Introduction

The spreading of liquid drops and films on a solid surface can be described by universal, 'macroscopic' laws [1] as soon as the thickness of the drop or film exceeds a few tens of nanometers. One such law is the so-called Tanner law, characteristic of the spontaneous spreading of small non-volatile drops on a flat substrate in a situation of complete wetting (see figure 1). After an initial transient regime, the base radius R of such a drop grows as $R \sim t^{1/10}$. The law has been derived analytically [2–4] and confirmed experimentally on many accounts [3, 5–7]. The fundamental argument is that the hydrodynamics in the bulk of a drop are driven by capillary forces alone, which directly yields $R \sim t^{1/10}$ assuming a self-similar shape for the bulk, in the lubrication approximation [2, 3]. Alternatively, the trend can be regarded as a competition between the hydrodynamic dissipation (primarily in the contact line region of the drop) and an unbalanced capillary force [1, 4, 8, 9].

The Tanner law is quite robust and typically offers an accurate description of the life of a droplet—which spans a few hours for liquids with moderate surface tensions and viscosities—apart from initial and final transients. The initial transient corresponds, e.g., to the deposit of the droplet on the substrate, and lasts less than a second for regular liquids. As for the final state of spreading, for non-volatile droplets it is either a molecular film or a flat, bounded structure—a 'mesoscopic' pancake [1, 10–12]—which may be more favorable energetically than a molecular film. Pancakes occur when short-range substrate interactions promote dewetting, even though the overall situation is that of complete wetting [13]: although not very common, such structures have been observed experimentally [14]. The existence of a limiting configuration, with a finite value for the base radius R, implies that the late-time spreading dynamics typically slow down with respect to the Tanner law.

By contrast to the trend of arrested spreading, it has recently been observed that the Tanner stage $R \sim t^{1/10}$ can
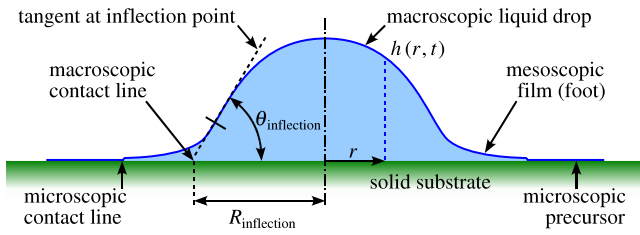
Figure 1. Cross-section of a circular droplet spreading in a situation of complete wetting (cartoon, color online). See section 2.1 for details.

be followed by a *faster* spreading law $R \sim t^\alpha$, with $\alpha > 1/10$. Specifically, for spontaneously spreading nematic liquid crystals [15, 16], the value of α was found to be nearly twice as large as the exponent $\alpha_{\text{Tanner}} = 0.1$ characterizing the Tanner law, with $\alpha = 0.2$ [15] and $\alpha = 0.19$ [16]. A more thorough analysis of the data suggests that the acceleration does not stop at $\alpha = 0.2$: values as high as $\alpha = 0.3$ can be observed at the end of the experiment. This 'accelerating' trend is apparently in conflict with the notion of a Tanner stage terminated by the onset of a molecular film or equilibrium pancake, and its physical origin has yet to be clarified.

We have already attempted a qualitative explanation of this post-Tanner trend in a macroscopic framework [17]. In the present paper, our goal is to account for the acceleration quantitatively and for this purpose we resort to the well-accepted thin film model (TFM). Analyzing the thin film equation (TFE) we see that at late spreading times the disjoining pressure dominates capillary effects. Then the local thickness $h(r, t)$ (see figure 1) obeys a diffusion equation, i.e., the whole droplet effectively becomes a diffusive film in the sense of Derjaguin [13]; the corresponding base radius R grows as $R \sim t^{1/2}$. Thus the experimentally observed transition from Tanner's law to power laws $R \sim t^\alpha$ with $\alpha \approx 0.2$ [15, 16] in fact seems to be part of a crossover to a much faster spreading law than expected previously. In order to validate this observation we integrate the TFE numerically, extract relevant observables and compare their evolution to the experimental data. We find the general trend illustrated by the 'numerical spreading' to be in good agreement with the spreading observed for nematic droplets in [15, 16]. However, our model has yet to take into account the typically non-Newtonian rheology of nematic liquid crystals. Our work in progress will address this effect in separate publications. The macroscopic interpretation of the acceleration in terms of a negative line tension is also provided elsewhere [17].

Our paper is organized as follows. In section 2 we give an overview of our system of interest and summarize previously attempted explanations for its abnormal spreading behavior. Section 3 features a brief derivation of the thin film equation and presents key analytical results that are directly relevant to the problem of nematic droplets. Section 4 focuses on key properties of our numerical spreading process (essentially a brute-force solution of the TFE), which is then compared quantitatively with physical experimental data in section 5. We conclude in section 6, relating our results to alternative concepts and providing outlook into our future work.

2. Overview of the problem

2.1. Anatomy of a spreading droplet: macroscopic versus mesoscopic

Figure 1 represents the quasistationary state of a spreading droplet, which is composed of: a 'macroscopic' liquid drop where shear is small and viscous forces are balanced primarily by variations of capillary Laplace pressure; a 'mesoscopic' part subject to large shear, where viscous forces are balanced primarily by variations of disjoining pressure; a 'microscopic' region featuring molecular precursor layers and a dry substrate [18, 19]. The relative sizes of these regions are not up to scale: the main purpose of figure 1 is to clearly distinguish the apparent contact line (typically inferred from the inflection point of the profile $h(r, t)$ at a given time t) from the 'real' contact line, governed by microscopic phenomena.

Most analyses assume that the macroscopic and mesoscopic scales are well-separated, i.e., that the bulk of the drop is much wider than the mesoscopic 'foot'. Thus the bulk is well approximated by a thin spherical cap with base radius $R(t)$, contact angle $\theta(t) \ll 1$ and nearly constant volume

$$V_{\text{cap}} = \frac{\pi}{4} R^3 \theta, \tag{1}$$

i.e., it is practically in equilibrium at constant volume V_{cap} and instantaneous base radius $R(t)$. In this approximation it is also customary to assimilate R and θ with their respective estimates inferred from the inflection point of $h(r, t)$, $R_{\text{inflection}}$ and $\theta_{\text{inflection}}$ (see figure 1), which can be obtained through optical observation of the apparent contact line [15, 16]. More immediately, these same optical experiments yield the location of the microscopic contact line (the characteristic thickness of which is 30 nm) and, e.g., $R_{\text{300 nm}}(t)$ such that $h(R_{\text{300 nm}}, t) = 300$ nm (see figures 2 and 4(a)). These measurements indicate that the length of the mesoscopic film ahead of the apparent contact line grows to millimetric sizes and becomes comparable with R at the end of the experiment. At this point the assumption of well-separated scales is clearly broken, and the macroscopic volume V_{cap} is significantly lower than the total volume

$$V = 2\pi \int_0^\infty h(r, t) r \, \mathrm{d}r. \tag{2}$$

2.2. Post-Tanner spreading laws: experimental evidence and tentative explanations

By contrast with previous evidence of Tanner's law, recent experimental studies of spontaneous spreading of nematic liquid crystals on hydrophilic [15] or hydrophobic [16] substrates revealed, after a transient Tanner stage, a surprising 'acceleration' (actually a spreading process that 'slows down more slowly' than the Tanner law). Figure 2 plots the relevant observables for one spreading experiment. The base radius R and contact angle θ were reportedly inferred from the inflection point of the thickness profile (see figure 1), although in fact the main observables were $R_{\text{30 nm}}$ and θ_{averaged} (see figure 4(a)) rather than $R_{\text{inflection}}$ and $\theta_{\text{inflection}}$. Initially [15] it was noted that Tanner's law crossed over to $R \sim t^\alpha$ with $\alpha \approx 0.2$.
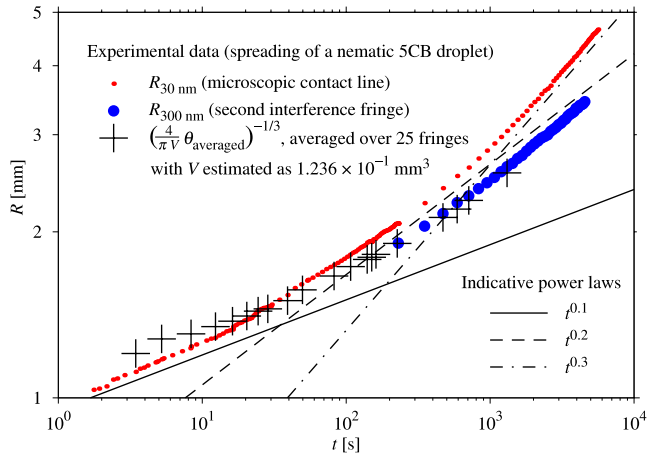
Figure 2. Overview of the 'accelerating' trend for a single spreading experiment (cyanobiphenyl 5CB droplet on silicon wafer). The quantities observed are $R_{30\,\text{nm}}$ (microscopic contact line; small dots, red online), $R_{300\,\text{nm}}$ (second interference fringe; big dots, blue online) and θ_{averaged} (slope averaged over 25 interference fringes; crosses). At $t > 200$ s the plot reveals the existence and growth of a large mesoscopic 'foot' at the edge of the droplet, comparable in size to the base radius (see figures 1 and 4(a)). It is also clear that both observed radii significantly deviate from Tanner's law $R \sim t^{1/10}$ and undergo a transient 'acceleration', past both the $R \sim t^{1/5}$ and $\sim t^{3/10}$ power laws. The volume V of the droplet was not measured directly but it can be estimated as $V = 1.236 \times 10^{-1}$ mm^3 (see sections 4.4 and 5).

It was also realized (see figure 4(b) in [15]) that the Tanner relation $\theta^3 \sim \text{Ca}$ (where $\text{Ca} \equiv \frac{\eta}{\sigma}\frac{\mathrm{d}R}{\mathrm{d}t}$ is the capillary number) does not hold for late spreading times: for small θ and Ca one has $\theta \sim \text{Ca}^{0.75}$. The latter relation, together with the volume conservation condition $R^3\theta \sim V$, is consistent with $R \sim t^{0.2}$. Similar results were reported for spreading on hydrophobic substrates (see figure 6 in [16]), with $\theta \sim \text{Ca}^{0.7}$ and $R \sim t^{0.19}$.

The conclusions from these results are as follows. On one hand [15], direct estimates of α through $R(t)$ are consistent with estimates via $\theta(\text{Ca})$, which apparently validates the hypothesis of an approximating spherical cap of constant volume (although the experimental data [15] offers no *direct* evidence for this). On the other hand, α is found to be significantly larger than the Tanner exponent $\alpha_{\text{Tanner}} = 0.1$. This signifies that some unknown factor, other than the surface tension, comes into play. Moreover, similar values of α were obtained for different kinds of substrates [15, 16], which suggests that the acceleration is a robust effect rather than an artifact, and an intrinsic feature of nematic droplets. One should also note that the experiment in [16] does not fully capture the post-Tanner transient and that exponents as high as $\alpha \approx 0.3$ are observed at late times (see figure 2).

Several qualitative arguments come to mind, which may or may not explain the reported acceleration. First of all, nematic crystals are known to have a non-Newtonian, shear-thinning rheology [20, 21]. Shear thinning affects the flow pattern and the dissipation rates and thus modifies the spreading dynamics, but it is not clear *a priori* whether the actual dynamics will be faster or slower than Tanner's power laws.

A detailed analysis of the contact line dynamics in the framework of the thin film model [22] shows that characteristic shear rates in the capillary wedge and in the mesoscopic precursor *decrease* as the contact line slows down, and thus for a non-Newtonian fluid the effective viscosity will *increase* with time. This corresponds to a modified spreading law $R \sim t^{\alpha}$ with $\alpha < 1/10$. Numerical experiments were carried out [23] and confirmed $\alpha < 1/10$ for shear-thinning fluids and $\alpha > 1/10$ for shear-thickening fluids. Thus the dominant effect from shear thinning is that the spreading is *slower* than predicted by Tanner's law, and we must seek another mechanism to explain the 'acceleration' observed for 5CB droplets.

Among other factors that could be responsible for an acceleration of spreading, we should also cite: (a) slippage at the substrate [24]; (b) somewhat counterintuitively, densely distributed roughness, which for small or zero contact angles causes wicking and 'enhances' the property of complete wetting [25]. Unfortunately, we must discard both these effects as possible causes of the observed acceleration in the case of our nematic droplets. First, slip has been shown to cause a logarithmically small contribution to the macroscopic spreading laws [24]; the acceleration observed in [15, 16] looks qualitatively different from a minor effect due to slip. As for roughness, the nematic droplets may encounter some anchoring defects on hydrophilic substrates [15], but hydrophobic substrates in [16] are definitely free of either chemical defects or topographic roughness; thus the consistent acceleration observed in both cases is not likely to be related to the 'superwetting' properties of rough substrates.

Finally, a very tempting approach is to describe the (non-volatile) system in terms of its total free energy. The 1985 review by de Gennes [1] has explained Tanner's law in terms of an effective driving force (derived from the instantaneous free energy). The work of the driving force is balanced by dissipation, primarily hydrodynamic dissipation in the macroscopic 'wedge' and mesoscopic 'foot' in the vicinity of the apparent contact line. The assumptions of this approach can be challenged by hypothesizing incomplete dissipation in the foot/precursor [15] or by introducing the concept of dynamic line tension, which contributes to the unbalanced Young force and plays a dominant role at long spreading times [17].

We note, however, that line tension as an equilibrium concept is quite subtle [26, 27] and its generalization to a quasistationary situation should not be taken lightly. It is also hard to derive a consistent set of correction terms for the hydrodynamic dissipation. More generally, the notion of a driving force acting on the edge of a macroscopic, capillary drop—this notion breaks down when the size of the mesoscopic region ('foot') becomes comparable to that of the bulk of the droplet, which is apparently the case during the reported acceleration (this is indicated, e.g., by the evolution of $R_{30\,\text{nm}}$ and $R_{300\,\text{nm}}$ on figure 2). This prompts us to describe the spreading droplet in a framework that resolves mesoscopic regions and does not use macroscopic approximations—the thin film model.

3. Thin film equation: presentation and analytical results

The thin film model (TFM)—related to both the 'interface displacement model' and the 'lubrication approximation'—is a continuum representation of the spreading dynamics, suitable for the study of thin films. While it may not accurately describe the spreading dynamics at molecular film thicknesses (see section 4.1), it is believed to work quite well for mesoscopic thicknesses, i.e., above several tens of nanometers. As opposed to macroscopic frameworks, the TFM accurately resolves quantities that would otherwise remain empirical, e.g., functionals of the thickness profiles in the vicinity of the apparent contact line and in the mesoscopic 'foot' of a droplet. Notably, Tanner's law was consistently derived in the framework of the TFM by Voinov [2], Tanner [3] and de Gennes [1, 4]. Numerous authors have since used the TFM to validate, refine, and generalize the features of advancing contact lines and, by extension, the spreading dynamics of droplets [28–30].

3.1. Thin film model as applied to nematic droplets

At the core of the framework is the thin film equation (TFE). The simplest expression of the TFE is for a Newtonian fluid with no slip at the substrate, in the approximation of small thickness gradients. In the following we briefly derive a TFE for nematic droplets.

We consider a quasistationary film of heterogeneous thickness $h(x, y)$ covering a homogeneous, flat substrate. Assuming that local equilibrium is achieved for all (x, y) and that the lateral flows in the film have negligible inertia (low Reynolds number), we can write the following energy functional:

$$\mathcal{E}[h] = \int \int \left[\sigma + \sigma_{\text{SL}} + \frac{\sigma}{2} (\nabla h)^2 + \Phi(h) \right] \mathrm{d}x \, \mathrm{d}y. \quad (3)$$

Here σ and σ_{SL} are the nominal surface energies of a free interface and of a solid–liquid interface, respectively, whereas $\Phi(h)$ is an effective interface potential acting as a correction to $\sigma + \sigma_{\text{SL}}$ due to the fact that h is finite. As for the excess energy due to the curvature of the free interface, it is well approximated with $\frac{\sigma}{2} \int \int (\nabla h)^2 \, \mathrm{d}x \, \mathrm{d}y$ in the small-slope approximation $|\nabla h| \ll 1$. It is common to neglect hydrostatic contributions to (3) in situations of complete wetting [1, 30].

Considering $\mathcal{E}[h]$ under volume-preserving variations of h, the quasistationary internal pressure $p(x, y)$ is found to be of the intuitive form

$$p = -\sigma \Delta h - \Pi(h), \quad (4)$$

which is a combination of the typical 'capillary' Laplace pressure and of the 'disjoining' pressure $\Pi(h) \equiv -\partial_h \Phi(h)$. The lateral pressure gradient ∇p is relaxed through a so-called Poiseuille flow

$$\mathbf{j} = -\frac{h^3}{3\eta} \nabla p, \quad (5)$$

assuming a constant viscosity η and no slip at the substrate (for a derivation, see [1] or [30]). Finally, the conservation equation $\partial_t h = -\nabla \cdot \mathbf{j}$, together with (4) and (5), yields

$$\partial_t h = -\nabla \cdot \left\{ \underbrace{-\frac{h^3}{3\eta} \nabla \underbrace{[-\sigma \Delta h - \Pi(h)]}_{\text{pressure } p}}_{\text{lateral current } \mathbf{j}} \right\}. \quad (6)$$

Due to the different nature of the two contributions to the pressure p, it is appropriate to rewrite (6) as

$$\partial_t h = -\frac{\sigma}{\eta} \nabla \cdot \left(\frac{1}{3} h^3 \nabla \Delta h \right) + \nabla \cdot [D(h) \nabla h] \quad (7)$$

where

$$D = -\frac{h^3}{3\eta} \frac{\mathrm{d}\Pi}{\mathrm{d}h} \quad (8)$$

is the effective diffusion coefficient introduced by Derjaguin [13]. The expression of D contributes to the second-order term of (7) and plays a major role in the spreading dynamics at mesoscopic thicknesses. In a continuum representation, it is expedient to approximate the disjoining pressure $\Pi(h)$, and hence $D(h)$, with a dominant long-range contribution, while introducing a phenomenological boundary condition (effectively a cutoff) in the nanometric range. Previous studies [1, 4, 30] addressed the case of $\Pi(h) = \frac{1}{6\pi} A h^{-3}$, a single power law accounting for the cumulated effect of non-retarded van der Waals interactions for a film of finite thickness h (A being the Hamaker constant). However, in the case of antagonistically anchored nematic liquid crystals [15, 16], the dominant term is

$$\Pi = \tfrac{1}{2} K \delta^2 h^{-2}, \quad (9)$$

K being the bend-splay elastic constant and δ the angle by which the director rotates over the thickness of the film, i.e., the difference between the anchoring angles at both interfaces. Note that we only take into account the elastic energy in the bulk of the nematic; the anchoring energies (surface terms) are taken to be constant, i.e., we assume sufficiently strong anchoring at both interfaces with respect to the thickness of the film. Thus in our case (8) reduces to

$$D = \frac{K \delta^2}{3\eta}. \quad (10)$$

Interestingly, the elastic interaction typical of antagonistically anchored nematics yields a purely diffusive film in the sense of Derjaguin. To the best of our knowledge, this remarkable feature of a thickness-independent diffusion coefficient has not been emphasized previously.

When describing the spreading droplet as a whole (as opposed to assimilating the apparent contact line to a quasistationary hydrodynamic wedge [1, 4, 30]), it is appropriate to rewrite (7) in a *rotationally* invariant geometry, i.e., with h depending only on the distance r to the vertical axis of the droplet (see figure 1),

$$\partial_t h = -\frac{\sigma}{\eta} \frac{1}{r} \partial_r \left\{ \frac{1}{3} h^3 r \partial_r \left[\frac{1}{r} \partial_r (r \partial_r h) \right] \right\} + D \frac{1}{r} \partial_r (r \partial_r h). \quad (11)$$

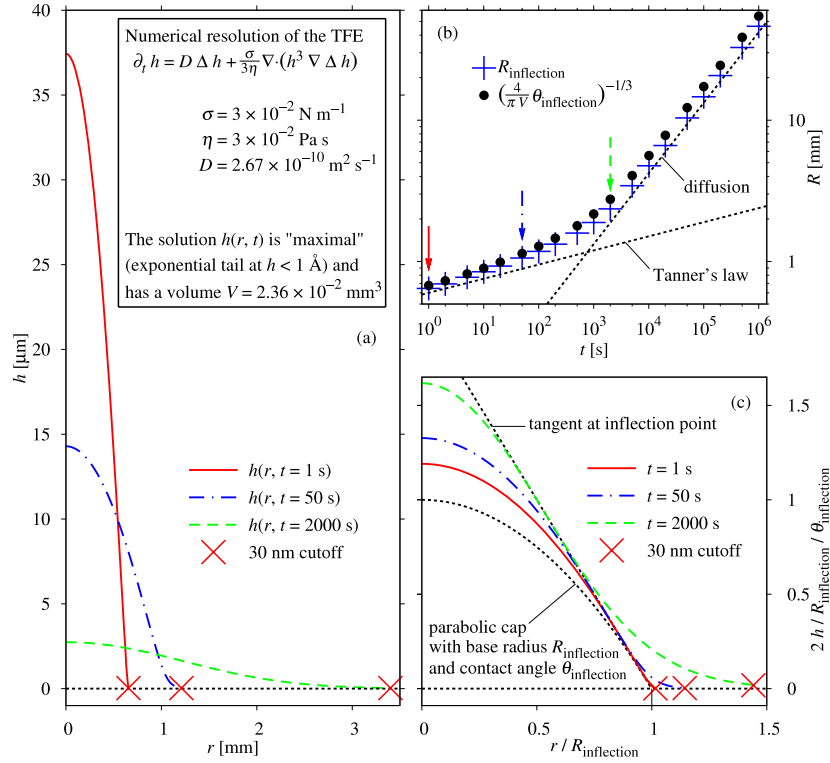Here we have used the fact that D is a constant for nematics.

Figure 3. Overview of the results of the numerical resolution of the thin film equation (TFE) with an 'elastic' contribution to the disjoining pressure, i.e., a diffusive second-order term: (a) three consecutive shapes adopted by a droplet of volume $V = 2.36 \times 10^{-2}$ mm^3 during a numerical spreading process (the oblique crosses indicate the points at which the solution $h(r, t)$ falls below $\varepsilon = 30$ nm, which is the characteristic thickness at the edge of the physical mesoscopic precursor [16]); (b) same experiment: time dependence of the base radius R of the drop, as estimated directly from the tangent at the inflection point (see figure 1) and also, tentatively, from the volume conservation law $V = \frac{\pi}{4} R^3 \theta$; (c) comparative analysis of the estimates of R and θ for the same cross-section snapshots as in (a): the tangent at the inflection point yields a sensible value for R, but θ does *not* correspond to an apex-fitting spherical cap, even at $t = 1$ s.

3.2. Asymptotic spreading behavior

Before we use (11) for quantitative predictions, we can make an important qualitative remark about the two limiting cases of the TFE. Looking at the two right-hand side terms of (7) or (11), for sufficiently tall droplets, the disjoining pressure $\Pi = \frac{1}{2} K \delta^2 h^{-2}$ is negligible with respect to the Laplace pressure over a large part of the droplet (the droplet is well approximated by a spherical cap as in section 2.1 and the Laplace pressure is $2\sigma\theta/R \simeq 2\pi[h(r = 0)]^2/V_{cap}$). In this approximation, the TFE is essentially fourth order and has the form

$$\frac{3\eta}{\sigma} \partial_t h = -\frac{1}{r} \partial_r \left\{ h^3 r \partial_r \left[\frac{1}{r} \partial_r (r \partial_r h) \right] \right\}. \qquad (12)$$

Looking for self-similar solutions of the form $h(r, t) = t^{-2\alpha} f(t^{-\alpha} r)$, with the scaling chosen so that $V = 2\pi \int h(r, t) r \, dr$ remains constant, (12) yields $\alpha = 1/10$, i.e., Tanner's law [2, 3, 28, 29].

It is also clear that at late stages of spreading, as the droplet becomes flatter, the Laplace pressure will eventually be dominated by the disjoining pressure, and the TFE (cf (7) and (11)) will be essentially second order, governed by the specific liquid–substrate interactions:

$$\partial_t h = \frac{1}{r} \partial_r [r D(h) \partial_r h]. \qquad (13)$$

In the nematic case, D has the constant expression (10) and an obvious self-similar solution of (13) is a Gaussian bell defined by

$$h(r, t) = \frac{V}{4\pi D t} \exp\left(-\frac{r^2}{4 D t}\right), \qquad (14)$$

with an arbitrary origin for time. The base radius and contact angle as inferred from the inflection point are $R = \sqrt{8Dt}$ and $\theta = \frac{4V}{\pi\sqrt{e}} R^{-3}$, so that the volume conservation relationship is $V = \sqrt{e}\frac{\pi}{4} R^3 \theta$, as opposed to $V = \frac{\pi}{4} R^3 \theta$ for the idealized Tanner regime.

Thus we see that the spreading process must cross over from an initial spreading phase, consistent with the generic Tanner's law, to another regime, specific to antagonistically anchored nematic liquid crystals: we shall see in section 4.4 that the characteristic time of the crossover scales as $T = (\frac{\sigma}{\eta} V^3 / D^5)^{1/4}$. The late-time evolution of a droplet is expected to be *diffusive*, i.e., measurements of $R(t)$ will yield an 'acceleration' from $R \sim t^{1/10}$ to $\sim t^{1/2}$. The remaining problem is to establish the characteristics of the crossover and to compare it to the physical experiment.

4. Numerical integration of the TFE: preliminaries

We integrated (11) in the form of a numerical spreading process, taking snapshots of the solution $h(r, t)$ at preset time intervals (figure 3(a)). The numerical values used were $\sigma =$
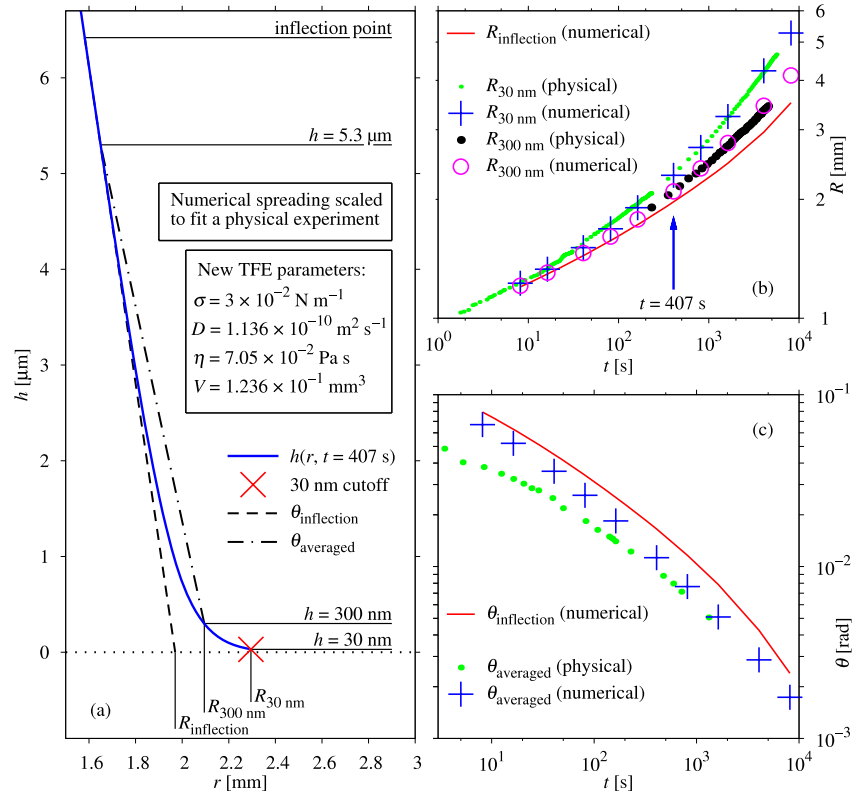
Figure 4. Quantitative fit of a physical spreading experiment (cyanobiphenyl 5CB on silicon wafer) in terms of the numerical spreading process presented in figure 3: the volume V and viscosity η act as scaling parameters of the maximal solution obtained previously (see text). (a) Illustrates the optically measured radii $R_{30\ nm}$ (at the edge of the mesoscopic precursor) and $R_{300\ nm}$ (corresponding to the second of a series of interference fringes), as well as the optically measured estimate of the contact angle $\theta_{averaged}$ (averaged over 25 fringes). Clearly $R_{inflection} < R_{300\ nm} < R_{30\ nm}$ and $\theta_{inflection} > \theta_{averaged}$. (b) Illustrates the good agreement for $R_{30\ nm}$ and $R_{300\ nm}$. (c) Compares estimates of the contact angle, with a satisfactory agreement at late spreading times, and a discrepancy at early spreading times.

30×10^{-3} N m^{-1}, $\eta = 30 \times 10^{-3}$ Pa s and $K\delta^2 = 12 \times 10^{-12}$ J m^{-1} (i.e., $D = 2.67 \times 10^{-10}$ m^2 s^{-1}). As for the boundary conditions, below $h = 1$ Å we extrapolate $h(r,t)$ as an exponential tail (similar to a 'maximal film' [1, 4, 30]) and ensure that the total volume $V = 2\pi \int h(r,t)r \, \mathrm{d}r$ is preserved: in figure 3, $V = 2.36 \times 10^{-2}$ mm^3. As for the initial conditions, we start with a perfect parabolic cap, to which we add a moderately smooth foot to avoid a computationally heavy singularity. Integration is explicit in time, with a fixed-size grid for r and an adaptive time step.

Figure 3(b) plots the spreading versus time in terms of the base radius R and contact angle θ, as inferred from the inflection point of $h(r,t)$ (see figures 1 and 3(c)). The volume of the numerical droplet is similar to the physical experiment [16], as well as the characteristics $\sigma = 30 \times 10^{-3}$ N m^{-1}, $\eta = 30 \times 10^{-3}$ Pa s and $K\delta^2 = 12 \times 10^{-12}$ J m^{-1}. The acceleration agrees qualitatively with figure 2 (cf figure 5 in [16]): the crossover from the Tanner phase to significantly faster regimes occurs at times of the order of a minute, for a droplet of the same 'caliber' as in [16] ($R \simeq 1$ mm at $t = 1$ s); a characteristic time of the crossover corresponds to the intersection of the asymptotes in figure 3(b), at $t \simeq 700$ s (about 12 min).

Before comparing quantitatively the physical spreading experiment with our numerical resolution of the TFE, we shall voice a few words of caution about the applicability of the TFM. We shall also review the physical observables available to us. Finally, we shall discuss the issue of time origin in spreading experiments and the scaling feature of equation (11).

4.1. TFM applicability

The oblique crosses on figures 3(a) and (c) indicate the points at which the solution $h(r,t)$ falls below $\varepsilon = 30$ nm, which is the characteristic thickness at the edge of the physical mesoscopic precursor [16]. For $t = 2000$ s (dash–dotted profile), $h(r = 0) \simeq 100\varepsilon$, thus the maximal solution $h(r,t = 2000$ s), as a continuum construct, is at the limit of physical relevance. We also note that the experimentally observed spreading dynamics of a similar 5CB droplet typically stop after an hour, with R of the order of tens of millimeters (which corresponds to a pancake of volume $V \simeq 10^{-2}$ mm^3 and thickness 30 nm). This behavior is due to short-range interactions which promote dewetting, and cannot be captured by the TFE (11) unless the expression (9) is refined. However, we *do* expect the TFE to capture the relevant properties of the contact line region as observed experimentally by Cazabat *et al* [15, 16], provided that the 30 nm thickness plays the role of a cutoff, located in the asymptotic region of $h(r,t)$ as is still the case for $t = 2000$ s on figures 3(a) and (c).

4.2. Review of the observables

Figure 3(c) makes it clear that the crossover from Tanner's law to a faster regime (at times of the order of a minute to an hour) coincides with a gradually lesser separation between the macroscopic and mesoscopic scales. In other terms, the extent of the mesoscopic 'foot' of the drop as compared to the macroscopic 'cap' is such that the apparent contact line is ill defined. Another, somewhat unexpected fact shown by figure 3(c) is that measuring the contact angle $\theta_{\text{inflection}}(t)$ at the (mesoscopic) inflection point of $h(r, t)$ does not give a good estimate of θ for the (macroscopic) apex-fitting spherical cap, even in the Tanner phase (at $t = 1$ s) and despite a seemingly good separation of the scales. This observation, however, does not challenge our study, provided that we complement R, θ, $R_{\text{inflection}}$ and $\theta_{\text{inflection}}$ with additional observables that are consistent with those measured by Cazabat *et al* [15, 16].

As a matter of fact, the optical measurements in [15, 16] do not infer R and θ from the inflection point, which would have required a thorough reconstruction of the profile at the contact line for each snapshot. It was more expedient to track the edge of the spreading drop (located at an approximate thickness of 30 nm; we shall note this radius $R_{30 \text{ nm}}$) or the second interference fringe of the ordinary–extraordinary coincidence pattern (at a thickness of about 300 nm; we shall note this thickness $R_{300 \text{ nm}}$). As for the contact angle, the slope at the contact line was averaged over the first 25 interfringes of the same pattern (between 300 nm and 5.3 μm). The numerical counterparts to these observable characteristics are presented in figure 4(a), on a representative snapshot of the numerical spreading process. We note that the interference pattern used here is specific to nematics: the fringes correspond to coincidence between the ordinary and extraordinary rays, and the interfringe is about 11 times larger than for the normal equal-thickness fringes.

4.3. Time origin of spreading processes

Both physical and numerical spreading processes can be seen as subject to initial conditions such as the deposit of a drop. Typically, shortly after a sufficiently compact deposit, flow patterns appear at the edge of the drop and propagate throughout the initially static droplet, establishing Tanner's regime; at later times, the spreading crosses over to, e.g., a diffusive phase (for nematic droplets with antagonistic anchoring, as considered in this paper; cf figure 3(b)).

The physically relevant deposit is closely related to the subtle issue of choosing a time origin ($t = 0$). On one hand, the exact history of the deposit has no effect at the scale of the long spreading process. On the other hand, the power law behavior typically observed in spreading is best represented in log–log diagrams (figures 2, 3(b), (c), 4(b), (c)), which are quite sensitive to the origin of t at small spreading times.

Thanks to the robust presence of a Tanner stage at early spreading times, the dilemma is customarily resolved by describing the spreading in terms of the time elapsed since the effective origin of the Tanner phase: practically, for a sufficiently compact deposit, the origin of t is slightly adjusted so that, e.g., $R(t)$ is well fit by a $t^{1/10}$ power law

at early spreading times. This may seem arbitrary but is in fact fundamental in the sense that for increasingly compact deposits of a given volume V the spreading processes converge towards a well-defined limiting process, which (at least in the framework of thin film dynamics) precisely corresponds to a backwards extrapolation of Tanner's law. This convention is adopted for both the physical and numerical spreading processes presented in this paper.

4.4. Scaling

A prominent feature of the model TFE (11) is that the equation can be scaled in terms of h, r and t (which corresponds to three degrees of freedom on σ, η, D and V). If we know a function $h_0(r, t)$ that is a solution of

$$\partial_t h_0 = -\frac{\sigma_0}{\eta_0} \frac{1}{r} \partial_r \left\{ \frac{1}{3} h_0^3 r \partial_r \left[\frac{1}{r} \partial_r (r \partial_r h_0) \right] \right\} + D_0 \frac{1}{r} \partial_r (r \partial_r h_0) \tag{15}$$

bearing the volume $V_0 = 2\pi \int_0^\infty h(r, t) r \, dr$, then we can define

$$k \equiv (V/V_0)^{1/8} \tag{16}$$

$$m \equiv \left(\frac{\sigma_0 \eta D}{\sigma \eta_0 D_0} \right)^{1/8} \tag{17}$$

$$n \equiv \left(\frac{\sigma_0 \eta D^5}{\sigma \eta_0 D_0^5} \right)^{1/4} \tag{18}$$

and obtain a similar function $h(r, t) = k^2 m^2 h_0(k^{-3} m r, k^{-6} n t)$ which is a solution of (11) with volume V.

In the work presented here, besides the obvious fitting in terms of the volume V via $k = (V/V_0)^{1/8}$, we assumed that the surface tension σ and the elastic coefficient $K\delta^2$ were not significantly different from the values $\sigma = 30 \times 10^{-3}$ N m^{-1} and $K\delta^2 = 12 \times 10^{-12}$ J m^{-1}. We allowed, however, for an adjustment in terms of the effective viscosity η, whereby $m = 1$ and $n = \eta_0/\eta$. Indeed, the rheology of a nematic film with antagonistic anchoring conditions is not as trivial as the Poiseuille flow in our model TFE: the effective viscosity must be intermediate between that of flow-aligned 5CB molecules (30×10^{-3} Pa s) and that of flow-orthogonal molecules (100×10^{-3} Pa s) [20, 21]. This also affects the value of the effective diffusion coefficient $D = \frac{K\delta^2}{3\eta}$. The results of the fit are $\eta = 70.5 \times 10^{-3}$ Pa s, $D = 1.136 \times 10^{-10}$ m^2 s^{-1} and $V = 1.236 \times 10^{-1}$ mm^3.

From the scaling factors k and n we conclude that the 'characteristic time' of the crossover for the TFE (11) scales as $T = (\frac{\sigma}{\eta} V^3/D^5)^{1/4}$. For the numerical values yielded by the fit we have $T \simeq 8 \times 10^4$ s (about 22 h), which exceeds by far the duration of the physical experiment (2 h). From the intersection of the asymptotes on figure 3(b) (at $t \simeq 700$ s) and the values $k = 1.23$ and $n = 0.425$ we can extract a more quantitatively relevant time $T = 5.7 \times 10^3$ s, i.e., a couple of hours rather than a day. Both values are consistent with the fact that the crossover to a diffusive spreading process is far from complete at the end of the observation in [16].

5. Comparison of physical and numerical spreading processes

We shall now perform a quantitative matching between the physical and numerical spreading processes. We adjusted the scaling of the numerical solution to accommodate the physical experiment, shifting the volume to $V = 1.236 \times 10^{-1}$ mm^3 and the viscosity to $\eta = 7.05 \times 10^{-2}$ Pa s. Then, for this rescaled numerical experiment, we measured the same quantities as observed optically, namely $R_{30\text{ nm}}$, $R_{100\text{ nm}}$ and θ_{averaged} (see figure 4(a)). The results are presented in figures 4(b) and (c).

The best agreement was obtained for $R_{30\text{ nm}}$, over the whole range where the two experiments overlap. As for the measurements based on interference patterns, the agreement is less consistent. On one hand (figure 4(b)), the radius $R_{300\text{ nm}}$ of the second interference fringe agrees well with its numerical estimate. On the other hand (figure 3(c)), at small spreading times the numerical θ_{average} is in excess of the optically observed slope averaged over the first 25 interfringes. The latter discrepancy may be due either to the low resolution of the fringes at early spreading times or to our failure to capture complex shear-thinning effects in the framework of the TFM.

Although the agreement is quite satisfactory for the $R_{30\text{ nm}}$ observable, we must note that the numerical estimate of $R_{30\text{ nm}}$ is at the limit of applicability of the TFM. In our model we simply cut off the maximal solution of the TFE at the thickness $h = 30$ nm, and the dynamics of this cutoff line may differ from the actual dynamics of the mesoscopic precursor near the microscopic contact line. It would be more conclusive if the physical experiment had systematically provided the more robust observables $R_{\text{inflection}}$ and $\theta_{\text{inflection}}$.

6. Conclusion

We have attempted an explanation of the abnormal spreading properties observed for small droplets of 5CB nematic liquid crystals [15, 16] in the framework of the thin film model. This approach enabled us to illustrate both qualitatively and quantitatively the key trends in the spreading of nematic droplets.

- The development of a large 'foot' (mesoscopic precursor), whereby the macroscopic and mesoscopic length scales are no longer well-separated.
- The transition towards a faster spreading regime—determined by the antagonistic anchoring of the nematic at the interfaces—in which the thickness profile is essentially governed by a diffusion equation.

The 'acceleration', initially observed optically by Cazabat *et al* [15, 16], was reproduced in a numerical spreading process (figure 3), which was used to fit the optical data (figure 2). The primary optical observable being the edge of the mesoscopic precursor, the agreement is satisfactory (figure 4(b)).

We note that this post-Tanner regime is *a priori* not specific to nematic droplets. Similar crossovers to faster spreading laws than $R \sim t^{1/10}$ may be observed for regular liquids dominated by van der Waals forces, although perhaps

not as readily as in the present case, where the spreading is driven by elasticity. The fundamental result is that, for long-range substrate interactions, the droplet essentially becomes a diffusive film in the sense of Derjaguin [13] at late spreading times, and Tanner's law is gradually replaced with another law, determined by the substrate interaction rather than by capillarity.

The work presented is a necessary complement to the quasistationary energetic approach as presented in [17], where acceleration is interpreted in terms of a dynamic, negative line tension τ attributed to the apparent contact line (see figure 1). The latter framework is applicable if the macroscopic and mesoscopic length scales remain well-separated, i.e., if the bulk of the droplet is well approximated by a spherical cap, and if both the vertical and lateral size of the mesoscopic region remain negligible. In this case, it is possible to isolate a line contribution, which resides in the mesoscopic 'foot', yet contributes to spreading dynamics at the macroscopic scale. However, as the droplet spreads, it eventually adopts a characteristic bell shape, and the capillarity-dominated spherical cap ceases to be a good approximation. At even later stages, the droplet may reach the state of a mesoscopic pancake, which cannot be resolved by the macroscopic model at all, unless the dimension is lowered to a planar geometry.

By contrast, the thin film model appears to be a more robust description of complete wetting situations, especially in the late stages of spreading. In order to account for the emergence of pancakes, we aim to provide the thin film equation with suitable boundary conditions that would account for the phenomenology of the microscopic contact line. As a prospect of future work, we also note that our current implementation of the thin film model does not accurately describe the non-Newtonian rheology of antagonistically anchored nematics. In future studies we may refine the notion of effective viscosity and allow for a more accurate modeling of the spreading dynamics.

References

[1] de Gennes P G 1985 *Rev. Mod. Phys.* **57** 827–63
[2] Voinov O V 1976 *Fluid Dyn.* **11** 714–21
[3] Tanner L H 1979 *J. Phys. D: Appl. Phys.* **2** 1473–84
[4] Hervet H and de Gennes P G 1984 *C. R. Acad. Sci., Paris* II **299** 499–503
[5] Ausserré D, Picard A M and Léger L 1986 *Phys. Rev. Lett.* **57** 2671–4
[6] Cazabat A M and Cohen-Stuart M 1986 *J. Phys. Chem.* **90** 5845–9
[7] de Ruijter M, De Coninck J and Oshanin G 1999 *Langmuir* **15** 2209–16
[8] Cazabat A M 1987 *Contemp. Phys.* **28** 347–64
[9] Léger L and Joanny J F 1992 *Rep. Prog. Phys.* **57** 431–86
[10] Ruckenstein E 1982 *J. Colloid Interface Sci.* **86** 573–4

[11] Joanny J F and de Gennes P G 1984 *C. R. Acad. Sci., Paris* II **299** 279
[12] Joanny J F and de Gennes P G 1984 *C. R. Acad. Sci., Paris* II **299** 605–8
[13] Derjaguin B V, Churaev N V and Muller V M 1987 *Surface Forces* (New York: Consultants Bureau, Plenum)
[14] Cazabat A M, Fraysse N, Heslot F, Levinson P, Marsh J, Tiberg F and Valignat M P 1994 *Adv. Colloid Interface Sci.* **48** 1–17
[15] Poulard C and Cazabat A M 2005 *Langmuir* **21** 6270–6
[16] Poulard C, Voué M, de Coninck J and Cazabat A M 2006 *Colloids Surf.* A **282** 240–6
[17] Mechkov S, Cazabat A M and Oshanin G 2009 Post-Tanner stages of droplet spreading: the energy balance approach revisited *J. Phys.: Condens. Matter* **21** 464131
[18] Burlatsky S F, Oshanin G, Cazabat A M and Moreau M 1996 *Phys. Rev. Lett.* **76** 86–90
[19] Burlatsky S F, Oshanin G, Cazabat A M and Moreau M 1996 *Phys. Rev.* E **54** 3832–45
[20] Nakano K 2003 *Tribol. Lett.* **14** 17–24
[21] Nakano K 2006 *Lubr. Sci.* **15** 233–52
[22] Carré A and Eustache F 2000 *Langmuir* **16** 2936–41
[23] Starov V M, Tyatyushkin A N, Velarde M G and Zhdanov S A 2003 *J. Colloid Interface Sci.* **257** 284–90
[24] Brochard-Wyart W, de Gennes P G, Hervert H and Redon C 1994 *Langmuir* **10** 1566–72
[25] McHale G, Shirtcliffe N J, Aqil S, Perry C C and Newton M I 2004 *Phys. Rev. Lett.* **93** 036102
[26] Schimmele L, Napiórkowski N and Dietrich S 2007 *J. Chem. Phys.* **127** 164715
[27] Mechkov S, Oshanin G, Rauscher S, Brinkmann M, Cazabat A M and Dietrich S 2007 *Europhys. Lett.* **80** 66002
[28] Diez J A, Gratton R, Thomas L P and Marino B 1993 *Phys. Fluids* **6** 24–33
[29] Diez J A, Gratton R, Thomas L P and Marino B 1993 *J. Colloid Interface Sci.* **168** 15–20
[30] Eggers J and Stone H A 2004 *J. Fluid Mech.* **505** 309–21